Data-driven design of biometric composite metamaterials with extremely recoverable and ultrahigh specific energy absorption

Zhenyang Gao[a,b], Hongze Wang[a,b,c*], Nikita Letov[d], Yaoyao Fiona Zhao[d,*], Xiaolin Zhang[a,b], Yi Wu[a,b,c,*], Chu Lun Alex Leung[e,f], and Haowei Wang[a,b,c]

[a]*State Key Laboratory of Metal Matrix Composites, Shanghai Jiao Tong University, Shanghai, 200240, China*

[b]*School of Materials Science and Engineering, Shanghai Jiao Tong University, Shanghai, 200240, China*

[c]*Institute of Alumics Materials, Shanghai Jiao Tong University (Anhui), Huaibei, 235000, China*

[d]*Department of Mechanical Engineering, McGill University, Montreal, H3A 0C3, Canada*

[e]*Department of Mechanical Engineering, University College London, London WC1E 7JE, UK*

[f]*Research Complex at Harwell, Harwell Campus, Oxfordshire OX11 0FA, UK*

[*]*This is to indicate the corresponding author, email: hz.wang@sjtu.edu.cn, yaoyao.zhao@mcgill.ca, eagle51@sjtu.edu.cn*

Abstract

The existing mechanical metamaterials are often designed with periodic inter-connected structs with simple cylindrical or uniform hierarchical geometries, which relies on their parent materials to either have a good mechanical performance with low recoverability, or significantly sacrifices their mechanical performances to be highly recoverable. Biological fibrous structures are often evolved with a composition of different fibrous morphologies to possess a desired balance of mechanical performances and recovery. In this study, we developed digital design algorithms to generate the next-generation metamaterials with composite bio-inspired twisting fibrotic structs that are rubber-like recoverable without significant scarification of their mechanical performances. A machine learning predictive model is trained based on experimental data to reveal the resulted specific energy absorption (SEA) and SEA recoveries for such metamaterials with complicated fiber-composition mechanisms. To further understand the fundamental structural recovery mechanisms of the natural fibers, we derived the elastoplastic theories of the twisting fibrotic structs, and revealed that such structs possesses a rubber-like fracture strain with significantly improved specific energy absorption. Our studies combined the structural recovery mechanisms of the composite natural fibrous structures and mechanical metamaterials, liberates the design potential of materials with engineerable optimal balances of their mechanical performances and recoverability.

Keywords: metamaterials, bio-inspired, machine learning, specific energy absorption, additive manufacturing, energy recovery

1. Introduction

Mechanical metamaterials are often referred to the materials with artificially engineered three-dimensional microstructures that possess remarkable mechanical properties, *e.g.* lightweight [1], ultrahigh stiffness [2-4], vibration mitigation [5], negative Possion's ratio [6, 7], fracture resistant [8, 9], and energy absorption [10-12]. Depending on the printing techniques and functional requirements, the existing metamaterials are often designed with patterns of interconnected cylindrical structs such as octet-truss [13], octahetral [14], body-centered-cubic (BCC) [15], or face-centered-cubic (FCC) [16], and fabricated with variety of parent materials ranging from rubber-like plastics to brittle ceramics [17]. Influenced by the design patterns of structs and the parent materials [18, 19], the metamaterials usually exhibits either good mechanical performances with a low recoverability [20, 21] or largely sacrifice their mechanical performances (*e.g.* stiffness, toughness, energy absorption) to achieve high recoverability [22-24]. For certain protective applications such as defensive armor or impact-resistant landing components of satellites, absorbing the mechanical energy from a secondary impact after recovering from the initial damages is desired (e.g. the secondary impact-landings of the satellites or rovers). Among the existing designs of the metamaterials however, a general design paradigm is missing to engineer the metamaterials to simultaneously achieve high recoverability and initial energy absorption. Current design strategies to improve mechanical performance of metamaterials include solid-hardening [25], crack guiding [26], or the functional grading [27, 28], the geometry and design of the struts in these metamaterials are simple and unable to provide significant improvement on mechanical performances whilst maintaining a high recoverability. Therefore, engineering next-generation mechanical metamaterials with tailored mechanical performance and high recoverability would require the fundamental breakthrough of their prematurely yielded struct designs.

In nature, protective biological structures are evolved to possess mechanical properties with structural recovery capabilities to resist mechanical damages induced from their surroundings. For example, the copra of the coconut is protected by the husk structure composed of twisting coir fibers with different fiber angles and numbers to against multiple impacts. Such natural fibers are widely observed in different natural species such as hemp [29], bamboo [30], and palms [31], which is lightweight [32], recoverable [33, 34], and damage-resistant [35, 36]. The underlying mechanisms of their structural recovery capability are worthwhile to be understood to reinforce existing struct design of metamaterials, and to create next-generation of metamaterials with tailored mechanical performances

with high recovery. Therefore, we propose a natural-fiber-inspired (NFI) strategy to replace the existing designs of structs for metamaterials, so that these materials can be rubber-like recoverable without scarification of its initial energy absorption. To achieve lattice materials with such novel and complicated structures, digital design algorithms including the NFI struct generation algorithm and composite NFI lattice generation algorithm are developed. To predict the mechanical properties of such metamaterials with a large number of highly abstract design parameters however, the conventional finite element analysis (FEA) or experimental approach consumes a large amount of computational or manual resources, which makes them impractical to aid the design process for the metamaterials with a highly controlled and optimized mechanical performances. As a maturing prediction tool, machine learning (ML) is widely applied in industrial designs [37, 38] and materials sciences [39, 40] to predict the future data based on uncovered patterns of data without deriving the analytical solutions or performing time-consuming simulations [41]. Therefore, we further proposed a innovative data-driven deep search optimization strategy enabled by ML to optimize the mechanical properties of the complicated metamaterials with composite compositions of struct morphologies based on the rapid property-predictions for thousands of design. Based on this optimization algorithm, we discovered a linear stiff-soft transition trend of NFI metamaterials that links the conventional stiff and soft phases of the material properties, which provides a useful design guideline to design the metamaterials with desired and optimal balance of SEA and SEA recoverability. As a result, the developed data-driven NFI metamaterials has a 6 to 36x and 6 to 16x higher initial SEA and recovered SEA compared to the lattice material fabricated by the rubber-like parent materials, while possess a 0.2 to 1.5x improvement of recovered SEA with similar initial SEA values for stiff parent materials.

A general research flowchart is provided in Fig. 1. Due to the consideration of computational cost, we used abstracted design data (NFI compositions) within the FCNN training process and optimization algorithm, while the printable files are generated by the NFI design algorithms. Specifically, the RGM deep search optimization algorithm uses a trained fully connected neural network (FCNN) as the fast prediction tool to search the optimal NFI compositions based on comparing the predicted mechanical properties from thousands of different NFI compositions. The design algorithms are used as the file-generation tool that takes the abstract design data as input, and generate the printable optimal data-driven NFI lattices with given optimal NFI compositions, or provides the training NFI lattices based on the training NFI configurations. Within the NFI design algorithms, the composite NFI lattice generation

algorithm uses the NFI struct generation algorithm as struct generation tool to convert the digital design matrix to a printable NFI lattice geometry. Inspired by the microstructure of natural fibers, we rebuild the structs of metamaterials with hierarchical twisting fibers based on the proposed composite NFI lattice generation algorithm in Section 2.1. The mechanical properties of the natural fibers are affected by its fibrous twisting structures and anisotropic mechanical behaviors of the monofilaments, where we focus on investigating structural effects of the natural fiber instead of its parent materials in this research. Therefore, we used stereolithography (SLA) technique to prepare the samples with smaller number of potential defects and mechanical instabilities of as-built materials from other techniques for a better precision of fabricating such complex geometry. Future study could further innovate the printing techniques to replicate the parent materials of natural fibers by fabricating the samples with engineerable and 3D-variable anisotropic local mechanical properties in different locations. Similar to the biological structures, we developed natural-fiber-inspired (NFI) lattices with composite fibrous morphologies, where each fibrous morphology represents the NFI structs with different number of fibers or fiber angles. We experimentally measured the initial specific energy absorption (SEA) and SEA recovery to reflect the mechanical performance and recovery of the specimens, respectively. Therefore, we designed the experiments to testify the specific energy absorption (SEA) of the initial and secondary compressions of the conventional and NFI lattice structures. To reveal the underlying effects of the percentages of fibrous morphologies on the resulting SEA and SEA recovery, we trained a fully connected neural network based on the experimentally gathered training data in Section 2.2. In Section 3.1, a random-generation-modified (RGM) deep search algorithm is combined with the FCNN to find the optimal percentages of fibrous morphologies within the NFI lattice that led to the highest recoverability with different initial SEAs. By deriving the data-driven percentages of fibrous morphologies for different levels of energy absorption performances, we discovered a highly recoverable linear stiff-soft transition phase of the metamaterials with well-performed mechanical energy absorptions. This linear stiff-soft relationship can also be used to precisely engineer metamaterials with an optimal balance between the mechanical energy absorption and recoverability. To explain such performances, the elastoplastic behaviors of fibrotic structs with different fiber parameters are elucidated based on theoretical and simulation efforts in Section 3.2, which indicates that the structs of NFI lattice exhibits a rubber-like mechanical recoverability with a 370 times higher SEA.

We provide data-driven strategies revealing the structural recovery mechanisms of composite natural

fibers, and derived fundamental elastoplastic theories of fibrotic structs. We replicate such structural recovery mechanisms from nature to the metamaterial design, successfully engineer next-generation artificial fibrous structures that are rubber-like recoverable with ultrahigh mechanical performances, through a data-driven approach.

2. Materials and methods

2.1. Digital design and fabrication of NFI lattice materials

Mimicking the helical microstructures of the coconut coir fibers (Fig. 2a), the structs of cubic NFI lattice specimens are developed based on a NFI struct generation algorithm with 3 × 3 × 3 arrangement of the unit cells and fabricated through SLA technique with Formlabs® Tough 2000 resin (See Fig. 2b, Supplementary Fig. 1 and Supplementary Information Section A). All NFI specimens are post-processed under same conditions (See Supplementary Table 1, and the Supplementary Information Section A), where the parent material exhibits an elastic modulus E = 1.31 GPa, yields at 3.46% with a yield stress σ_y = 26.01 MPa, and fails at 33.03% with a fracture strength σ_f = 34.41 MPa (Fig. 3, Table 1). The unit cells of the specimens are designed with the octet-truss microstructure due to its profound energy absorption capabilities [21, 42], and a cell size of 10 mm.

The design of the NFI structs (Fig. 4) includes four steps: (1) the convertibility analysis, where original conventional structs are categorized to either convertible or inconvertible structs; (2) the NFI conversion, where the design curves of NFI structs are generated; (3) the design of structural relations, where appropriate relations among the fiber number n, fiber diameter d_f, fiber separation distance d_s, node diameter D, and the node minima area A_{minima} are established for a consistent cross-sectional area of the struct, and an improved printability. The morphology of the NFI structs (Fig. 2a, Fig. 5) is engineered with twisting fibers of fiber angles in the range $17^{\circ} \leq \theta_f \leq 57^{\circ}$ and fiber numbers ranging from 1-3. To determine the convertibility of a conventional struct (Fig. 5), the maximum fabrication angle of its potential NFI fibers is calculated based on the summation of the structural angle θ_s and the fiber angle θ_f. It is then compared with the printability limit of the fabrication platform θ_p to determine whether the unsupported minima would occur. Note that the unsupported minima represent the regions that are unable to be fabricated without the additions of internal support structures, where these support structures are difficult to be removed for complicated lattice structures. For a convertible struct where the maximum fabrication angle is below θ_p, groups of control points C_1 to C_m are developed to generate the

NFI curves (Fig. 6). To derive the control points within each group, an initial control point $p_{1,1}$ and its mirror point $p_{1,1,\text{mirror}}$ are constructed with respect to the central axis of C_1 to C_m with equation (1-3) satisfied:

$$l\,(p_{1,1}, p_{1,1,\text{mirror}}) \perp l\,(O_1, O_m) \tag{1}$$

$$O_1 \in l\,(p_{1,1}, p_{1,1,\text{mirror}}) \tag{2}$$

$$d\,(p_{1,1}, p_{1,1,\text{mirror}}) = d_s \tag{3}$$

where $l\,(x, y)$ represents the line with x and y as its edge points, $d\,(x, y)$ is the distance between x and y, O_i is the center of the control point circle C_i. Based on constraints from equation (1-2), we initialize the coordinate of $p_{1,1}$ and $p_{1,1,\text{mirror}}$ as:

$$p_{1,1} = (x_{o_1} + y_{o_2} - y_{o_1},\ y_{o_1} + x_{o_1} - x_{o_2},\ z_{o_1}) \tag{4}$$

$$p_{1,1,\text{mirror}} = (x_{o_1} + y_{o_1} - y_{o_2},\ y_{o_1} - x_{o_1} + x_{o_2},\ z_{o_1}) \tag{5}$$

To ensure the constraint of the separation distance (equation (3)), the coordinate of $p_{1,1}$ is adjusted by:

$$p_{1,1} = O_1 + d_s/d(p_{1,1}, p_{1,1,\text{mirror}})(p_{1,1} - O_1) \tag{6}$$

According to these implementations, the initial control point $p_{i,1}$ of each control point group C_i is derived by:

$$p_{i,1} = p_{1,1} + [(i-1)/(m-1)](O_m - O_1) \tag{7}$$

For the NFI struct with fiber number n, the adjacent control points in each group are separated at an angle:

$$\theta_c = 2\pi/n \tag{8}$$

Therefore, the j^{th} control point $p_{i,j}$ on C_i is implemented based on the rotational operation from the rhinoscriptsyntax library [43]:

$$p_{i,j} = R(p_{i,1}, (j-1)\theta_c, \overrightarrow{O_1 O_m}) \tag{9}$$

where $R(p, \theta, \overrightarrow{xy})$ represents the rotational operator to rotate the point p with an angle θ based on the rotational axis $\overrightarrow{xy}$. To obtain the twisting feature of the NFI structs, secondary rotational operations are applied for each point group C_i based on the fiber angle θ_f:

$$C_i = R(C_i, \Delta\theta, \overrightarrow{O_1 O_m}) \tag{10}$$

$$\Delta\theta = [2(i-1)d(O_1, O_m)]/)/[(m-1)\cos\theta_f\, d_s] \tag{11}$$

where $\Delta\theta$ is the angle of rotation calculated based on equation (11). Trough connecting $p_{1,j}$ to $p_{m,j}$ for each j, the curves of the NFI structs are constructed. To preserve a uniform cross-sectional area of the NFI structs for comparison purposes (Fig. 7), equation (12) is assured:

$$nd_f^2 = d_c^2 \quad (12)$$

where d_f and d_c are the diameters of the NFI fiber and conventional struct, respectively. Based on this calculation, the radius of the fibers is in the range 202 μm ≤ r_f ≤ 350 μm with a separation distance of d_s = 1000 μm between the fiber centers, which are engineered to produce a consistent cross-sectional area of the structs. This consistency requires the total cross-sectional areas of the NFI structs with different number of fibers sums to that of the conventional struct with a 350 μm radius, since further reducing this radius will results in fiber diameter lower than 200 μm, and will leads to a print failure. To form the connections between NFI structs, the unsupported minima is removed from spherical nodes (Fig. 7), where the cross-sectional area of the minima A_{minima} is derived as:

$$A_{\text{minima}} = \pi[(d_s - d_f)/2]^2 \quad (13)$$

Finally, the NFI curves are solidified into solid structures, and merged with the nodes upon the calculated structural relations (Fig. 8).

To design a composite NFI lattice with the desired composition of NFI struct morphologies, a composite NFI lattice generation algorithm (Fig. 9) is developed in the Python environment and applied as a Rhino plug-in to create desired design files. The algorithm can be subdivided into three processes: (1) calculation of the total struct numbers based on the given NFI composition; (2) generation of the 3D design matrix based on the random coordinate assignments; (3) creation of the composite NFI lattice material using the NFI struct generation algorithm (Fig. 4 to Fig. 8). For a given percentage composition of the NFI struct morphologies $\{p_0, p_1, \dots, p_{15}\}$ (Fig. 10, also refer to Table 2 for the design information of struct morphologies), the corresponding struct numbers are derived by

$$\{N_0, N_1, \dots, N_{15}\} = N \times \{p_0, p_1, \dots, p_{15}\} \quad (14)$$

where $\{N_0, N_1, \dots, N_{15}\}$ are the number of the NFI structs with different morphologies within the composite NFI lattice material, N is the total number of convertible structs for a given lattice configurations:

$$N = C_x C_y C_z N_{\text{unit cell}} - N_{\text{unconvertible}} \quad (15)$$

where $N_{\text{unit cell}}$ is the number of the struct segments for a given unit cell topology, $N_{\text{unconvertible}}$ is the number of unconvertible structs derived based on the convertibility analysis (Fig. 5), C_x, C_y, C_z are the cell numbers of a lattice material in x, y, and z directions in Cartesian coordinates, respectively. Afterward, $N_0, N_1, \dots, N_{15}$ random coordinates from the lattice materials are selected without duplications and assigned for the design parameters of struct morphology 0 to morphology 15,

respectively, to form the 3D design matrix (Fig. 9) of composite NFI lattice. Based on the distribution of θ_f and n on the design matrix, the NFI struct generation algorithm is applied for each individual struct to generate the corresponding NFI structs at desired locations of the lattice materials.

2.2. Machine learning studies of the composition of fibrous morphologies

Due to the complex microstructures of the NFI lattice material, the computational cost of predicting its mechanical performances is unacceptable through the traditional finite element analysis (FEA) approach. It is also not realistic to develop analytical solutions of the NFI specimen, because it is composed of in total 756 structs with 16 different types of NFI morphologies (fiber number $n = 1,2,3$, and fiber angle $\theta_f = 17^o, 27^o, 37^o, 47^o, 57^o$). Therefore, we developed a FCNN based on TensorFlow[44] to evaluate the initial SEA and SEA recovery of NFI lattice materials. The schematics of a sample training data gathering process is provided in Fig. 11. To experimentally characterize mechanical performances and recoveries of composite NFI lattice materials and construct the training data (Fig. 11a), the initial specific energy absorption (SEA) and SEA recovery values of NFI lattice specimens are calculated based on the experimental results from the energy recovery tests that consist of three steps: (1) an initial compression of the sample with a compressive displacement δ_0, where the initial SEA is recorded; (2) an one-hour structural recovery without loading; and (3) a secondary compression of the sample with a compressive displacement $\delta_0 - \delta_p$, where δ_p is the permanently deformed length along the compressive direction, and the SEA recovery is derived. Prior to the mechanical measurements, the specimens are secured in a dark environment after their fabrications to avoid the inconsistency of the ultraviolet exposure. During an energy recovery test, the samples are initially compressed to 40% of their height with a load rate of 2 mm/min to satisfy a quasi-static compressive condition, which is beyond the densification stage of the contacting layer for conventional octet-truss lattice used in this research (Video S1). During the recovery, the samples are released from the load, where the one-hour recovery time is chosen to ensure an abundant structural recovery. The calculation of initial SEA and SEA recovery is given by:

$$\text{Initial SEA} = \int_0^{\delta_0} F_{\text{I}}\, d\delta / m \tag{16}$$

$$\text{SEA Recovery} = \int_0^{\delta_0 - \delta_p} F_{\text{II}}\, d\delta / \int_0^{\delta_0} F_{\text{I}}\, d\delta \tag{17}$$

where m is the mass of the specimen, F_{I}, F_{II} are the loads during the initial and secondary compression, respectively. According to equation (16-17) a sample training data can be constructed (Fig. 11c), where the calculation logics are provided in Fig. 11d.

We applied the composite NFI generation algorithm to create NFI specimens with randomly distributed, artificially controlled percentages of different fibrous morphologies for training data construction. Based on the preliminary experiments, we observed that the composition of the fiber morphologies rather than their spatial distributions over the lattice structures has more contribution to the SEA and SEA recovery, where the composition of conventional structs have the most significant effect. Therefore, the training fibrous compositions are constructed with a fully covered percentage range of the conventional structs (0% to 100%), where the training data is evenly separated with different percentage compositions of conventional structs to improve the quality of the training process (Fig. 12). To ensure the sufficient amount of training samples, we gradually increase the quantity of the training samples until error of the predicted values converges (Fig. 13). Specifically, 80 sets of training data are experimentally constructed with the inputs as different percentages of fibrous morphologies, and the output as either the initial SEA or the SEA recovery. The structure of FCNN is composed of three hidden layers with 20 neurons in each layer, where the input layer with 16 percentages of fibrous morphologies is gradually connected into a single output unit (Fig. 14, Supplementary Information Section B). Separate training processes are performed to develop two neural networks for the predictions of SEA and SEA recovery. To avoid the vanishing gradient issue[45] caused by mapping a large input space into a small amount of outputs, the rectified linear activation function (ReLU) is constructed throughout the network to predict the mechanical performances of NFI lattices with non-saturating non-linearity natures:

$$a_j^i = \max(0, z_j^i) \tag{18}$$

$$z_j^i = \sum_{k=1}^{20} W_{jk}^i \, a_k^{i-1} + b_j^i \tag{19}$$

where z_j^i, a_j^i is the input and output values of the j^{th} neuron in i^{th} layer, respectively, W_{jk}^i is the weight of a_k^{i-1} on z_j^i, b_j^i represents the bias between the adjacent layers. In addition, comparison between different activation functions including the tanh, sigmoid, and ReLU (Supplementary Fig. 3) indicates the ReLU produces the best decay of the loss function during the training cycles.

To evaluate the trained model, we calculated and recorded the mean squared error loss function during the total 2000 training epochs and evaluated the accuracy of the model by 10% randomly selected test data (Fig. 15). The significant decrease of the loss functions attested the training quality of the FCNN, while the accuracy of the trained model is converged to a 10% and 5% error (Fig. 13) when compared to the test data, as the size of the training samples scales up. Based on the repetitive tests, the experimental values with standard deviations fits in the confidence intervals of predicted values for the initial SEA

(Fig. 16a) and SEA recovery (Fig. 16b), respectively, which ensured the reliability of the FCNN. Based on a trained ML model, the underlying relations between the mechanical performances and the compositions of fibrous morphologies are revealed, which enables the possibility of data-driven approaches of designing the NFI lattice material with optimal percentages for its fibrous morphologies.

3. Results and discussion

3.1. Data-driven design of NFI lattice material

Based on the ML prediction model, we used a data-driven approach to control the composition of fibrous morphologies to develop the NFI lattice material with optimal relation of initial SEA and SEA recovery properties. To search the optimal NFI composition for the highest SEA recovery of different initial SEA values, a ML-aided RGM deep search algorithm is developed (Fig. 17). Within each deep search cycle, 1000 random percentages $\{p_0, p_1, \dots, p_{15}\}_{1-1000}$ are generated, and the ML prediction model is applied to select the optimal composition that satisfies:

$$\text{maximize SEA Recovery}\{p_0, p_1, \dots, p_{15}\}_i \quad \text{s.t. SEA}\ \{p_0, p_1, \dots, p_{15}\}_i \geq \text{SEA}_{\text{target}}\ (i = 1, \dots, 1000) \quad (20)$$

where $\{p_0, p_1, \dots, p_{15}\}_i$ is the i^{th} randomly generated composition, $\text{SEA}_{\text{target}}$ is the minimum initial SEA value to be reached. According to the optimal composition, the composition range, R, of the random-generation is narrowed with a search-factor α for the next search cycle, and the optimization procedure terminates once the SEA recovery value converges or the range R reaches user-defined limit (Fig. 17, also see the Supplementary Fig. 4, as well as the Supplementary Information Section B, for the detailed comparison of computation efficiency among nested loop, deep search, and RGM deep search approaches). To explain, the increment limit of SEA recovery value is selected to match with the accuracy of the FCNN. The range limit could be determined based on the consideration of the computational cost or the resolution of the optimal NFI composition. In this study, the range limit is set as 0.1%, since further reducing the range will not results in differences of the number of NFI structs for each fibrous morphology.

Through searching the maximum SEA recovery for different initial SEA values, a linear relation between the initial SEA and the maximum SEA recovery is observed (Fig. 18a). In addition, the experimental results with standard deviations confirm with the confidence intervals of predicted values as expected. Apart from the traditional soft phase with reduced mechanical performance, or the stiff phase with low SEA recovery of the material design, we discovered and established a novel transition phase that connects the soft and stiff phase, where its relation between the initial SEA and SEA recovery

is described by:

$$\text{MAX (SEA Recovery)} = k_{\text{SEA}}\text{SEA} + b_{\text{SEA}} \quad (21)$$

where $k_{\text{SEA}} = -1.39 \times 10^{-2}$ g/mJ, b_{SEA} = 100.33% are the derived coefficients of the data-driven relation. The accuracy of this relation is validated through the experimental testing of seven data-driven NFI samples with the initial SEA ranging from 1000 mJ/g to 4000 mJ/g with 500 mJ/g spacing, which gives 4.6% and 7.2% average deviations for initial SEA and SEA recovery when compared to the predicted curve, respectively. Compared to the conventional octet-truss lattice material with an initial SEA of 4133 mJ/g and SEA recovery of 36%, the data-driven NFI lattice material can provide a 45% to 87% ultrahigh SEA recovery for initial SEAs reducing from 4000 mJ/g to 1000 mJ/g (see the Supplementary Video S1-5 for the experimental recordings and interactive mechanical curves for A-E in Fig. 18a).

The detailed fibrous compositions of the conventional lattice (E) and selected optimal NFI lattices (A-D) are provided in Fig. 18b. It is observed that a larger percentage composition of the conventional structs would result in a reduced SEA recovery and an improved SEA. Within the NFI transition phase, we further observed a uniform-to-composite transform of the NFI percentages at the initial SEA of 1500 mJ/g, where the deformation analysis of the samples is performed to reveal the underlying mechanisms (Fig. 18c). In the uniform NFI regime with an initial SEA below 1500 mJ/g, no conventional structs are required for the NFI lattice material (see Supplementary Fig. 5 for the initial SEA range of uniform NFI lattice materials), and the structural recovery reached 100% for a SEA recovery larger than 80%. To achieve such goal, the data-driven design algorithm avoids the constraining effects between the unrecoverable and recoverable grains of NFI structs for a well-distributed structural deformation during the initial compression, and a maximized structural recovery.

In the composite NFI regime, the NFI lattice material needs to involve a certain portion of conventional structs and the NFI structs with low $\varepsilon_{y,NFI}$ for a further improved initial SEA. In this case, the data-driven design algorithm is more interested to provide a design solution that possesses both high-recoverable grains and less-complaint grains of NFI and conventional structs, where the high-recoverable grains suffered the majority of the structural deformation and utilized the constraining effects to aid the recovery of less-complaint grains. Different from conventional octet-truss lattice material, this composite NFI lattice design allows a larger structural and SEA recovery potentials, which results in an improved SEA recovery with similar initial SEA values. These newly engineered stiff-soft transition

metamaterials can readily be applied in numerous applications where a precise control of the balance between the energy absorption and the softness is desired for customized demands (Fig. 19a), or a transition between the soft and stiff area is required to resist a large amount of impact while protecting the soft and vulnerable human bodies (Fig. 19b).

We directly compared the data-driven NFI lattice material and different state-of-the-art energy absorbing lattice materials designed with struct patterns including the face-centered-cubic (FCC), body-centered-cubic (BCC), vintiles, and octet-truss. The parent materials with both stiff/unrecoverable (Formlabs® Tough 2000) or soft/recoverable (Formlabs® Flexible 80A) mechanical properties are selected (Fig. 20, also see the Fig. 3 and Table 1 for the property of parent materials). Fig. 20a compared the recoverable SEA and initial SEA values for these lattice materials with the data-driven NFI lattice materials proposed in this work, we observed that the NFI lattice materials exhibits a 6 to 36x and 6 to 16x improvement for initial SEA and recovered SEA compared to the lattice material fabricated by the soft and recoverable Flexible 80A parent material. Compared to lattice materials prepared with Tough 2000 resin, the data-driven NFI lattice materials also possess a 0.2 to 1.5x improvement of recovered SEA with similar initial SEA values. For the SEA recovery ratio with different initial SEA (Fig. 20b), the data-driven NFI lattice materials have a 25% - 50% larger SEA recovery ratios for similar initial SEAs compared to Tough 2000 lattice materials, and exhibit a 1041% higher initial SEA for similar SEA recover ratios compared to Flexible 80A lattice materials.

3.2. Elastoplastic theory of NFI structs

To explain the excellent initial SEA and SEA recovery of NFI lattices, we performed theoretical derivations and simulations to reveal the structural recovery mechanisms of the NFI struct (Fig. 21 and Fig. 22). For the simulations, the struct models are generated using the NFI struct generation algorithm (Fig. 4 to Fig. 8) proposed in this work and designed with two cylindrical compressive plates at their edges. The models are imported into Abaqus CAE for deformation simulation, where the quasi-static simulation condition is selected. A fixed boundary condition is applied on the bottom plate of the NFI struct, while a forced displacement is designed on its top plate (Supplementary Fig. 7). In addition, the twisting structs are meshed using the 10-node quadratic tetrahedron (C3D10) mesh elements with an average mesh size of 0.2. The elastoplastic material properties (Fig. 3, Table 1) are assigned to the mesh elements based on experimental results. During the simulation, the stress and strain fields are recorded to compare with the theoretical calculations (Fig. 21a) and visualize the stress distribution (Fig. 21b).

The maximum strain of a NFI struct is reduced by an increased fiber number and fiber angle (see Supplementary Fig. 6, and Supplementary Information Section C, for detailed derivations), as described by:

$$\varepsilon_{NFI} = 1 - \cos\theta\sqrt{(1+\varepsilon)^2 + \tan^2\theta} \quad (22)$$

where ε_{NFI} is the maximum strain of the fibers, ε is the strain of the NFI struct, θ is the smallest structural angle of the NFI struct, given as:

$$\theta = \arccos(D\cos\theta_f/(D - 2\sqrt{An/\pi})) \quad (23)$$

where D is the separation distance between the fiber center, A is the total cross-sectional area of the struct, θ_f is the fiber angle, and n represents the fiber number. Based on equation (22), the effective yield and fracture strains of the NFI struct (Fig. 21a caption) is modelled by:

$$\varepsilon_{y,NFI} = \sqrt{(1+\varepsilon_y)^2/\cos^2\theta - \tan^2\theta} - 1 \quad (24)$$

$$\varepsilon_{f,NFI} = \sqrt{(1+\varepsilon_f)^2/\cos^2\theta - \tan^2\theta} - 1 \quad (25)$$

where ε_y, ε_f, $\varepsilon_{y,NFI}$, and $\varepsilon_{f,NFI}$ are the yield strain of conventional struct, fracture strain of conventional struct, effective yield strain of NFI structs, and effective fracture strain of NFI structs, respectively.

In linear elastic regime (Fig. 21a), the NFI structs proposed in this work are able to suffer a deformation strain 30% - 250% larger than conventional structs to permanent deformation, and exhibits a significant increment rate of $\varepsilon_{y,NFI}$ for a larger θ_f (equations (24) and (25)). The deformation simulation of the NFI structs at conventional yielding point indicated a more distributed and lower intensity of the stress field compared to the conventional structs, while a further reduction of the stress magnitude is observed for an increased fiber number n and fiber angle θ_f (Fig. 21b). This extended elastic range with well-distributed stress field explains the ultrahigh structural and SEA recovery of the NFI lattice compared to its conventional contour parts.

In the elastoplastic regime (Fig. 22), we calculated the normalized loads of the NFI structs and conventional structs prepared with different parent materials by:

$$F_{\text{normalized,NFI}} = \sigma(\varepsilon_{\text{NFI}}(\varepsilon), \text{MAT})A/m_{\text{struct}} \quad (26)$$

$$F_{\text{normalized,conventional}} = \sigma(\varepsilon, \text{MAT})A/m_{\text{struct}} \quad (27)$$

where m_{struct} is the mass of the interested struct, $\sigma(\varepsilon, \text{MAT})$ represents the stress of material type MAT at strain ε based on experimental stress-strain curves of the parent materials (Fig. 3), $F_{\text{normalized,NFI}}$ and $F_{\text{normalized,conventional}}$ represent the normalized loads for NFI and conventional structs, respectively. To obtain a high fracture strain, the conventional structs relies on the properties of the parent materials (Fig.

22a), which scarifies a significant amount of mechanical stiffness. However, the NFI structs (Fig. 22a) are able to withstand an unreduced normalized fracture load with an increased fracture strains controlled by θ_f and n. Compared to the conventional deceasing trend of SEA and fracture strain relations (Fig. 22b), the NFI structs provide an anomalistic increasing SEA with higher fracture strains. These fibrotic structs provide rubber-like facture strains, but possesses a 370 times higher SEA compared to the rubber-like flexible materials. The novel elastoplastic behavior of this biological structure leads to the fundamental controllable, highly recoverable, and significant SEA properties of the NFI lattices.

4. Conclusions

We identified the mechanical elastoplastic behavior of the biometric fibrous structures, and integrated different fibrous morphologies to form the mechanical metamaterials with extremely recoverable and ultrahigh mechanical performance through a data-driven approach, where the following conclusions are reached:

(1) The conventional metamaterials are unable to simultaneously achieve a high SEA and SEA recovery due to the early yielding or their structs, which makes them unfunctional after the initial resistance to the damage. We challenged this fundamental problem of the existing mechanical metamaterials by replacing their cylindrical or simple hierarchical structs with NFI structs to have with rubber-like recoverability but ultrahigh SEA, and confirms that the fundamental early yielding problems of the traditional structs can be successfully prevented by the anomalistic elastoplastic behavior of the novel twisting fibers.

(2) We developed composite NFI metamaterials with artificially engineered compositions of 16 different fibrous morphologies based on digital design algorithms that significantly utilized the design freedom offered by AM. However, conventional FEA or experimental approaches are unable to efficiently predict the mechanical properties of the metamaterials with such complicated structures for optimization purposes. In this study, we innovatively proposed a ML-aided deep-search optimization strategy that is able to generate the desired NFI configurations through predicting the SEA and SEA recoveries for thousands of abstracted information of NFI design updates, which makes it possible to design the complicated composite metamaterials with highly optimized and precisely controlled mechanical performances.

(3) Our paper used a data-driven approach to discover a linear stiff-soft transition phase of composite NFI metamaterials with different compositions of fibrous morphologies. This design guideline leads to

the next-generation metamaterials with engineerable balance of their SEA and recoverability, enduing a wide application potential for the proposed NFI metamaterials in different engineering practices such as the shoe sole or body-armor where a designable softness distribution is acquired.

(4) We developed a data-driven NFI metamaterials that have a significantly outperformed SEAs and SEA recoveries compared with existing metamaterial designs with different lattice structures fabricated with both stiff and soft parent materials. Indicated by the experimental results, a 6 to 36x and 6 to 16x higher initial SEA and recovered SEA is achieved compared to the lattice material fabricated by the rubber-like parent materials, while a 0.2 to 1.5x improvement of recovered SEA with similar initial SEA values is observed for stiff parent materials.

Our proposed mechanical metamaterials enable the potentials for (1) developing highly recoverable metamaterials with artificially controlled balance of mechanical performance and recoverability; and (2) forming a stiff-soft transition phase of the metamaterial with engineerable simultaneous improvements of its mechanical performance and recoverability. Our proposed methodology rationalizes new design, modeling, and experimental approach to understand and apply natural-fiber-inspired structural recovery mechanisms into mechanical metamaterials.

Acknowledgements

This work was sponsored by the National Natural Science Foundation of China (52075327 and 52004160); National Sciences and Engineering Research Council of Canada Discovery Grant (RGPIN-2018-05971); Shanghai Sailing Program (20YF1419200); Natural Science Foundation of Shanghai (20ZR1427500); and Major Science and Technology Project of Huaibei (Z2020001). The authors thank the facility access to the BL13HB beamline of Shanghai Synchrotron Radiation Facility (SSRF) and staff support.

References

[1] Tan C, Li S, Essa K, Jamshidi P, Zhou K, Ma W, et al. Laser Powder Bed Fusion of Ti-rich TiNi lattice structures: Process optimisation, geometrical integrity, and phase transformations. International Journal of Machine Tools and Manufacture. 2019;141:19-29.

[2] Zheng X, Lee H, Weisgraber TH, Shusteff M, DeOtte J, Duoss EB, et al. Ultralight, ultrastiff mechanical metamaterials. Science. 2014;344(6190):1373-7.

[3] Jiang H, Ziegler H, Zhang Z, Zhang H, Le Barbenchon L, Atre S, et al. 3D printed tubular lattice metamaterials for mechanically robust stents. Composites Part B: Engineering. 2022;236:109809.

[4] Ge J, Huang J, Lei Y, O'Reilly P, Ahmed M, Zhang C, et al. Microstructural features and compressive

properties of SLM Ti6Al4V lattice structures. Surface and Coatings Technology. 2020;403:126419.
[5] Chen Y, Wang L. Bio-inspired heterogeneous composites for broadband vibration mitigation. Scientific reports. 2015;5:17865.
[6] Yasuda H, Yang J. Reentrant origami-based metamaterials with negative Poisson's ratio and bistability. Physical review letters. 2015;114(18):185502.
[7] Babaee S, Shim J, Weaver JC, Chen ER, Patel N, Bertoldi K. 3D soft metamaterials with negative Poisson's ratio. Advanced Materials. 2013;25(36):5044-9.
[8] Da D, Chan Y-C, Wang L, Chen W. Data-driven and topological design of structural metamaterials for fracture resistance. Extreme Mechanics Letters. 2022;50:101528.
[9] Sadeghzade S, Emadi R, Salehi M, Tavangarian F, Ramini A. Crack propagation and toughening mechanisms of bio-inspired artificial spicules fabricated by additive manufacturing technique. Theoretical and Applied Fracture Mechanics. 2020;110:102797.
[10] Tancogne-Dejean T, Spierings AB, Mohr D. Additively-manufactured metallic micro-lattice materials for high specific energy absorption under static and dynamic loading. Acta Materialia. 2016;116:14-28.
[11] Dai M, Liang J, Cheng C, Wu Z, Lu J, Deng J. Large Deformation and Energy Absorption Behaviour of Perforated Hollow Sphere Structures under Quasi-Static Compression. Materials. 2021;14(13):3716.
[12] Gao Z, Wang H, Sun H, Sun T, Wu Y, Leung CLA, et al. Additively manufactured high-energy-absorption metamaterials with artificially engineered distribution of bio-inspired hierarchical microstructures. Composites Part B: Engineering. 2022:110345.
[13] Korshunova N, Alaimo G, Hosseini SB, Carraturo M, Reali A, Niiranen J, et al. Image-based numerical characterization and experimental validation of tensile behavior of octet-truss lattice structures. Additive Manufacturing. 2021;41:101949.
[14] Yan X, Li Q, Yin S, Chen Z, Jenkins R, Chen C, et al. Mechanical and in vitro study of an isotropic Ti6Al4V lattice structure fabricated using selective laser melting. Journal of Alloys and Compounds. 2019;782:209-23.
[15] Zhao M, Liu F, Fu G, Zhang DZ, Zhang T, Zhou H. Improved mechanical properties and energy absorption of BCC lattice structures with triply periodic minimal surfaces fabricated by SLM. Materials. 2018;11(12):2411.
[16] Wang P, Yang F, Li P, Zheng B, Fan H. Design and additive manufacturing of a modified face-centered cubic lattice with enhanced energy absorption capability. Extreme Mechanics Letters. 2021;47:101358.
[17] Shahzad A, Lazoglu I. Direct ink writing (DIW) of structural and functional ceramics: Recent achievements and future challenges. Composites Part B: Engineering. 2021;225:109249.
[18] Nazir A, Abate KM, Kumar A, Jeng J-Y. A state-of-the-art review on types, design, optimization, and additive manufacturing of cellular structures. The International Journal of Advanced Manufacturing Technology. 2019;104(9-12):3489-510.
[19] Yu X, Zhou J, Liang H, Jiang Z, Wu L. Mechanical metamaterials associated with stiffness, rigidity and compressibility: A brief review. Progress in Materials Science. 2018;94:114-73.
[20] Yuan S, Chua CK, Zhou K. 3D-printed mechanical metamaterials with high energy absorption. Advanced Materials Technologies. 2019;4(3):1800419.
[21] Song J, Zhou W, Wang Y, Fan R, Wang Y, Chen J, et al. Octet-truss cellular materials for improved mechanical properties and specific energy absorption. Materials & Design. 2019;173:107773.
[22] Hassan MS, Chavez LA, Chou C-C, Hall SE, Tseng T-L, Lin Y. Mechanical response of shape-

recovering metamaterial structures fabricated by additive manufacturing. Materials Research Express. 2021;8(11):115801.
[23] Park J-H, Park K. Compressive Behavior of Soft Lattice Structures and Their Application to Functional Compliance Control. Additive Manufacturing. 2020:101148.
[24] Weeger O, Boddeti N, Yeung S-K, Kaijima S, Dunn M. Digital design and nonlinear simulation for additive manufacturing of soft lattice structures. Additive Manufacturing. 2019;25:39-49.
[25] Pham M-S, Liu C, Todd I, Lertthanasarn J. Damage-tolerant architected materials inspired by crystal microstructure. Nature. 2019;565(7739):305.
[26] Gao Z, Li D, Dong G, Zhao YF. Crack path-engineered 2D octet-truss lattice with bio-inspired crack deflection. Additive Manufacturing. 2020;36:101539.
[27] Wo P, Zhao X, Munroe P, Zhou Z, Li K, Habibi D, et al. Extremely hard, damage-tolerant ceramic coatings with functionally graded, periodically varying architecture. Acta Materialia. 2013;61(1):193-204.
[28] Ren L, Wang Z, Ren L, Han Z, Liu Q, Song Z. Graded biological materials and additive manufacturing technologies for producing bioinspired graded materials: An overview. Composites Part B: Engineering. 2022:110086.
[29] Shahzad A. Hemp fiber and its composites–a review. Journal of composite materials. 2012;46(8):973-86.
[30] Liu D, Song J, Anderson DP, Chang PR, Hua Y. Bamboo fiber and its reinforced composites: structure and properties. Cellulose. 2012;19(5):1449-80.
[31] Elseify LA, Midani M, Shihata LA, El-Mously H. Review on cellulosic fibers extracted from date palms (Phoenix Dactylifera L.) and their applications. Cellulose. 2019;26(4):2209-32.
[32] Rangappa SM, Siengchin S. Lightweight natural fiber composites. Journal of Applied Agricultural Science and Technology. 2019;3(2):178.
[33] Ahmad F, Choi HS, Park MK. A review: natural fiber composites selection in view of mechanical, light weight, and economic properties. Macromolecular materials and engineering. 2015;300(1):10-24.
[34] Li M, Pu Y, Thomas VM, Yoo CG, Ozcan S, Deng Y, et al. Recent advancements of plant-based natural fiber–reinforced composites and their applications. Composites Part B: Engineering. 2020;200:108254.
[35] Elanchezhian C, Ramnath BV, Ramakrishnan G, Rajendrakumar M, Naveenkumar V, Saravanakumar M. Review on mechanical properties of natural fiber composites. Materials Today: Proceedings. 2018;5(1):1785-90.
[36] Chang X, Xu Q, Lv J, Xu L, Zhu Z, Liu S, et al. Bioinspired 3D helical fibers toughened thermosetting composites. Composites Part B: Engineering. 2021;216:108855.
[37] Gao Z, Dong G, Tang Y, Zhao YF. Machine learning aided design of conformal cooling channels for injection molding. Journal of Intelligent Manufacturing. 2021:1-19.
[38] Usuga Cadavid JP, Lamouri S, Grabot B, Pellerin R, Fortin A. Machine learning applied in production planning and control: a state-of-the-art in the era of industry 4.0. Journal of Intelligent Manufacturing. 2020;31(6):1531-58.
[39] Zeng S, Li G, Zhao Y, Wang R, Ni J. Machine learning-aided design of materials with target elastic properties. The Journal of Physical Chemistry C. 2019;123(8):5042-7.
[40] Chaudry UM, Hamad K, Abuhmed T. Machine learning-aided design of aluminum alloys with high performance. Materials Today Communications. 2021;26:101897.
[41] Murphy KP. Machine learning: a probabilistic perspective: MIT press; 2012.

[42] Ling C, Cernicchi A, Gilchrist MD, Cardiff P. Mechanical behaviour of additively-manufactured polymeric octet-truss lattice structures under quasi-static and dynamic compressive loading. Materials & Design. 2019;162:106-18.
[43] McNeel R. Rhinoceros 3D, Version 6.0. Robert McNeel. Associates: Seattle, WA, USA. 2010.
[44] Abadi M, Agarwal A, Barham P, Brevdo E, Chen Z, Citro C, et al. Tensorflow: Large-Scale Machine Learning on Heterogeneous Systems, Software. available from tensorflow org. 2015.
[45] Hochreiter S. The vanishing gradient problem during learning recurrent neural nets and problem solutions. International Journal of Uncertainty, Fuzziness and Knowledge-Based Systems. 1998;6(02):107-16.

Figures and tables

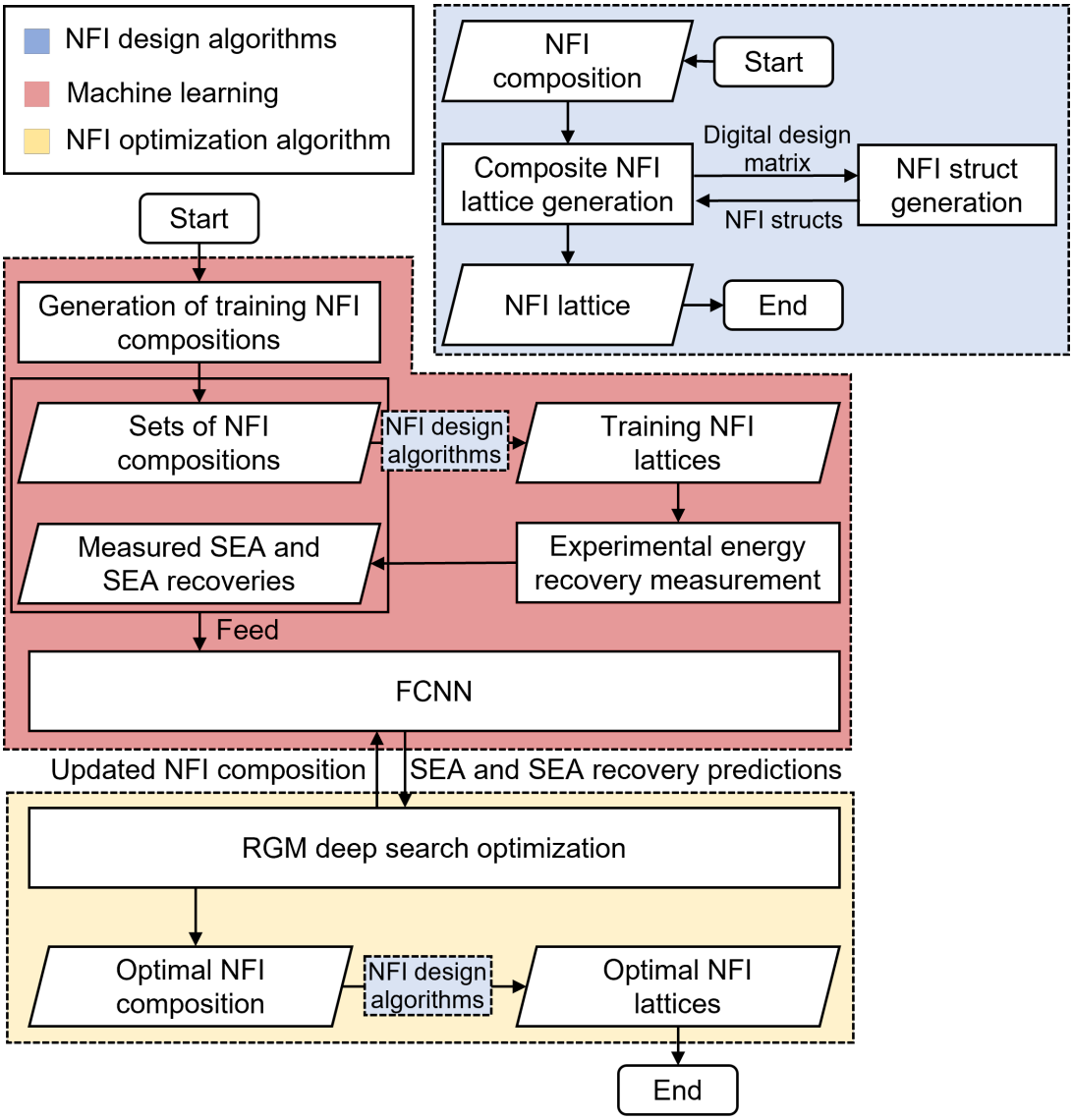

Fig. 1. Research flowchart of this paper, where the detailed descriptions of FCNN, NFI struct generation algorithm, composite NFI lattice generation algorithm, and RGM deep search optimization algorithm are provided in Fig. 4 to Fig. 8, Fig. 9 to Fig. 10, Fig. 11 to Fig. 15, and Fig. 17, respectively.

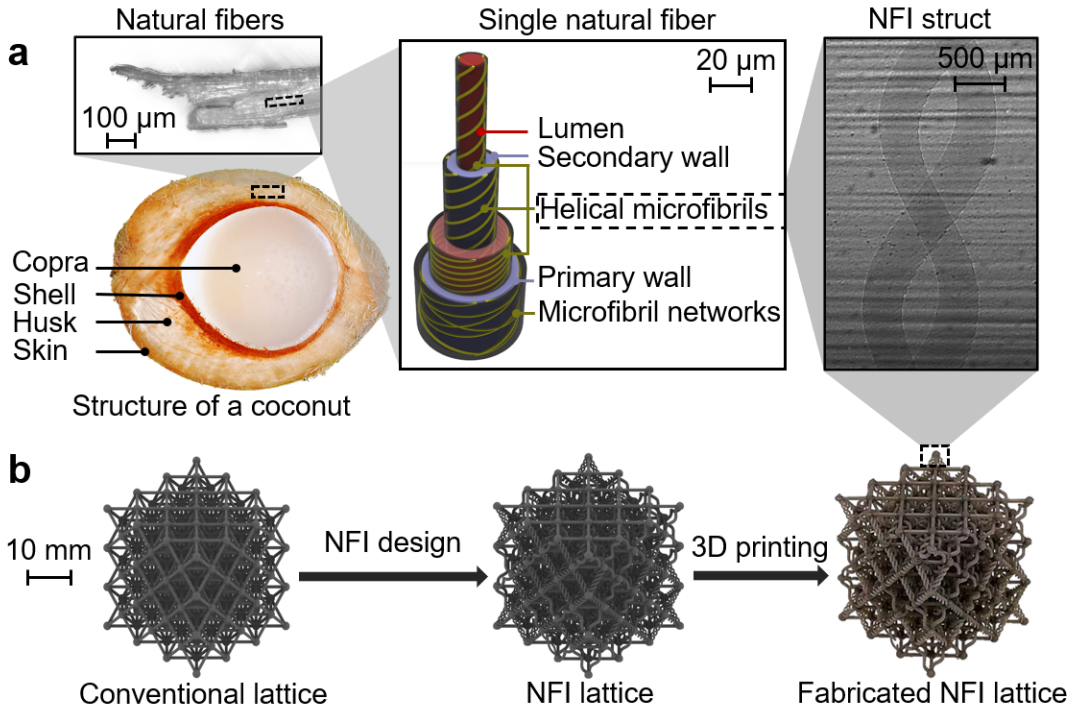

Fig. 2. Bio-inspired design and fabrication of NFI specimens: (a) the microstructure of the natural fiber and its design inspirations, where the single NFI struct are captured by in-situ X-ray technology; (b) the design and fabrication of NFI lattice.

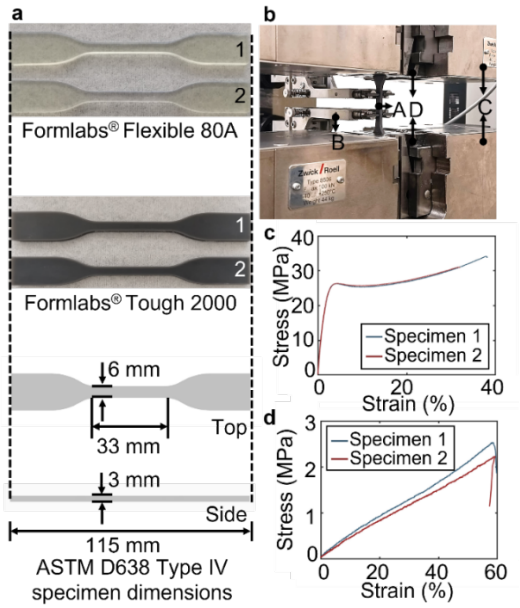

Fig. 3. Mechanical evaluations of parent materials: (a) design of the specimens; (b) experimental configurations, where A is the specimen to be tested, B is the extensometer for the strain measurement, C represents the load cells for the load application and measurement, D are the grips for the specimen holding; (c-d) the experimental stress-strain curves for Formlabs® Tough 2000 and Formlabs® flexible 80A parent material, respectively.

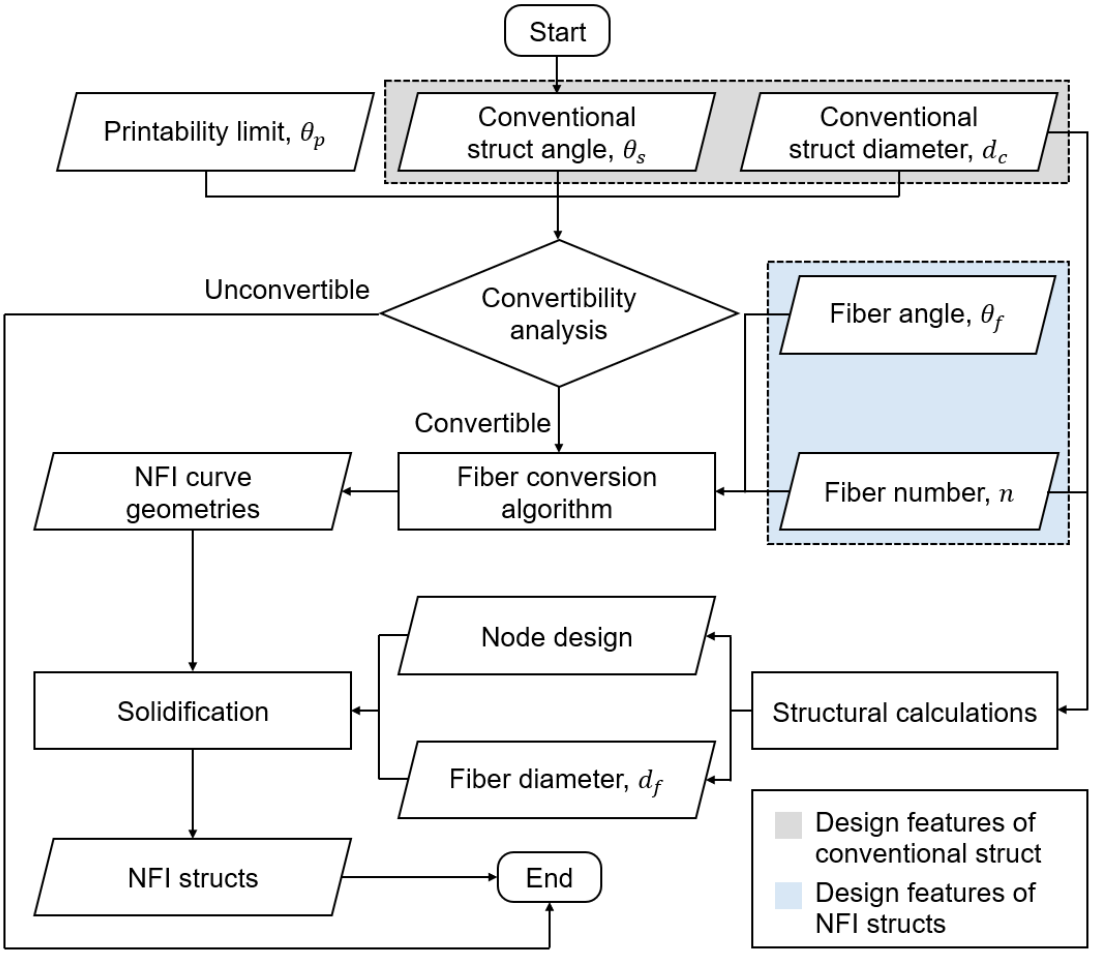

Fig. 4. Flowchart of NFI struct generation algorithm.

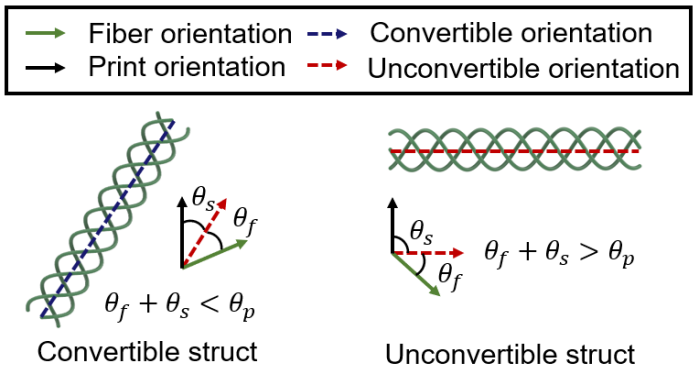

Fig. 5. The convertibility analysis, where $\boldsymbol{\theta_s}$, $\boldsymbol{\theta_f}$, $\boldsymbol{\theta_p}$ are the angles of the original struct, fiber, and printability limit to the print direction, respectively.

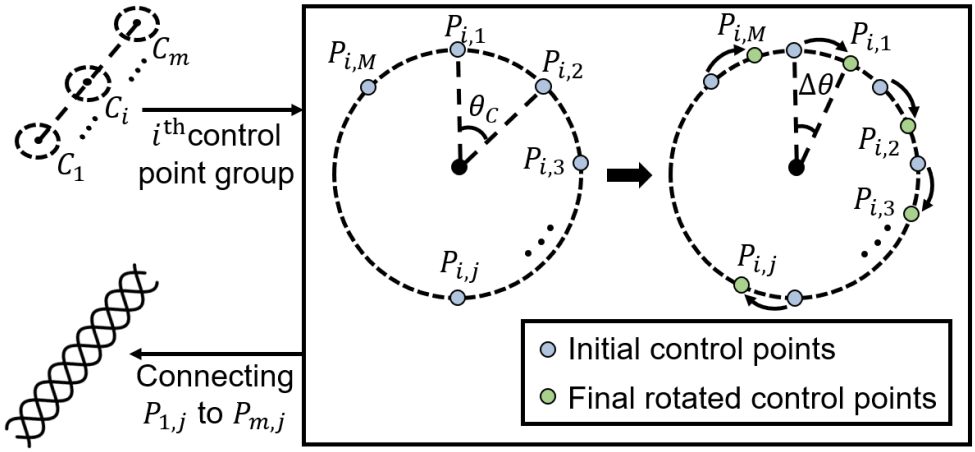

Fig. 6. The fiber conversion algorithm, where $\boldsymbol{p_{i,j}}$ represents the $\boldsymbol{j^{\text{th}}}$ control point on $\boldsymbol{i^{\text{th}}}$ circle of the control-point group $\boldsymbol{C_i}$.

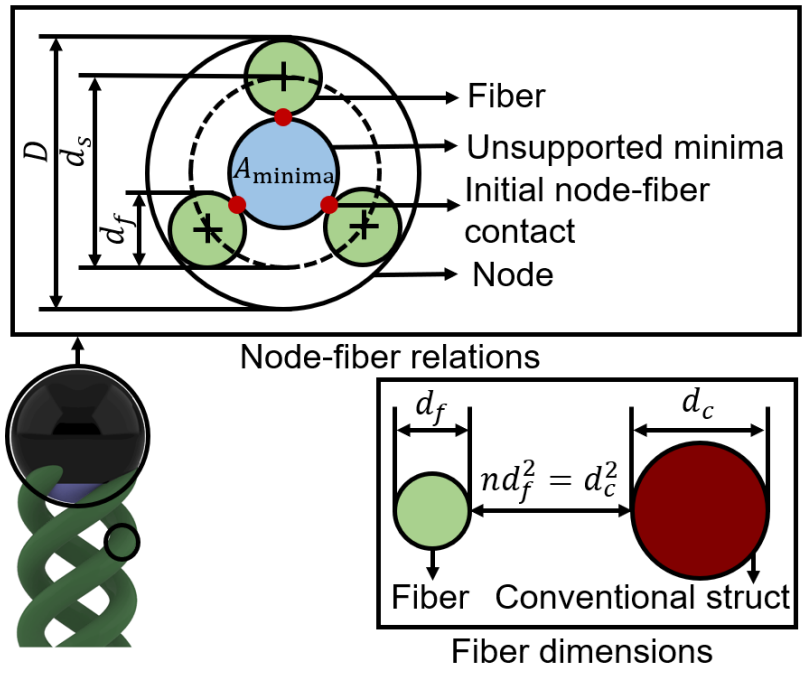

Fig. 7. The structural relations among the fibers, node, and conventional struct, where $\boldsymbol{D}$ is the diameter of the node, $\boldsymbol{d_s}$ is the separation distance of the centers of the fibers, $\boldsymbol{d_f}$ represents the diameter of the fiber, $\boldsymbol{d_c}$ is the diameter of the conventional struct, $\boldsymbol{A_{\text{minima}}}$ is the area of the node minima, and $\boldsymbol{n}$ is the fiber number.

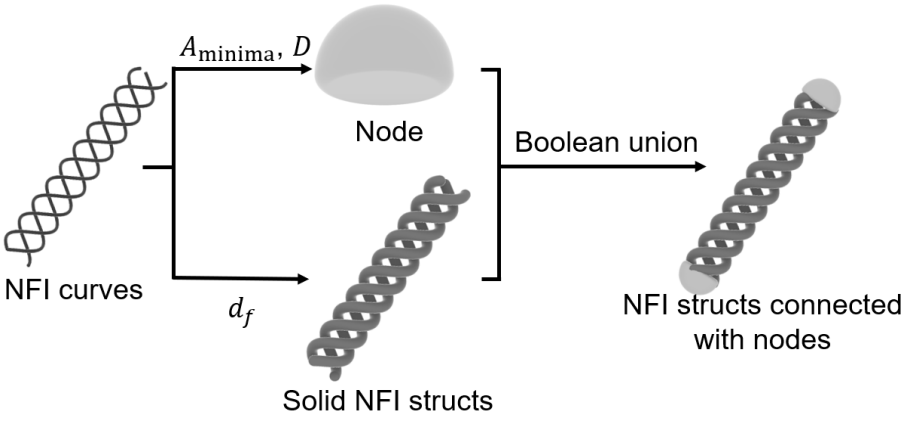

Fig. 8. The solidification process of the NFI struct.

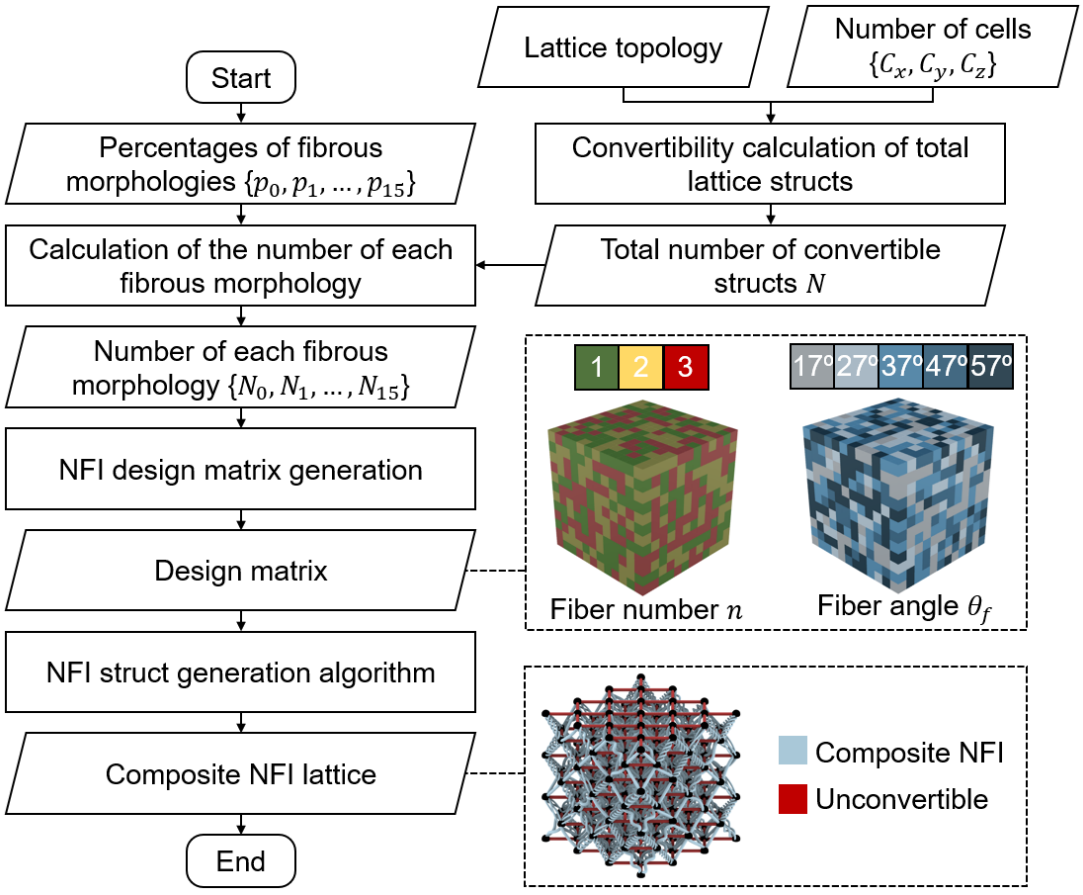

Fig. 9. The composite NFI lattice generation algorithm.

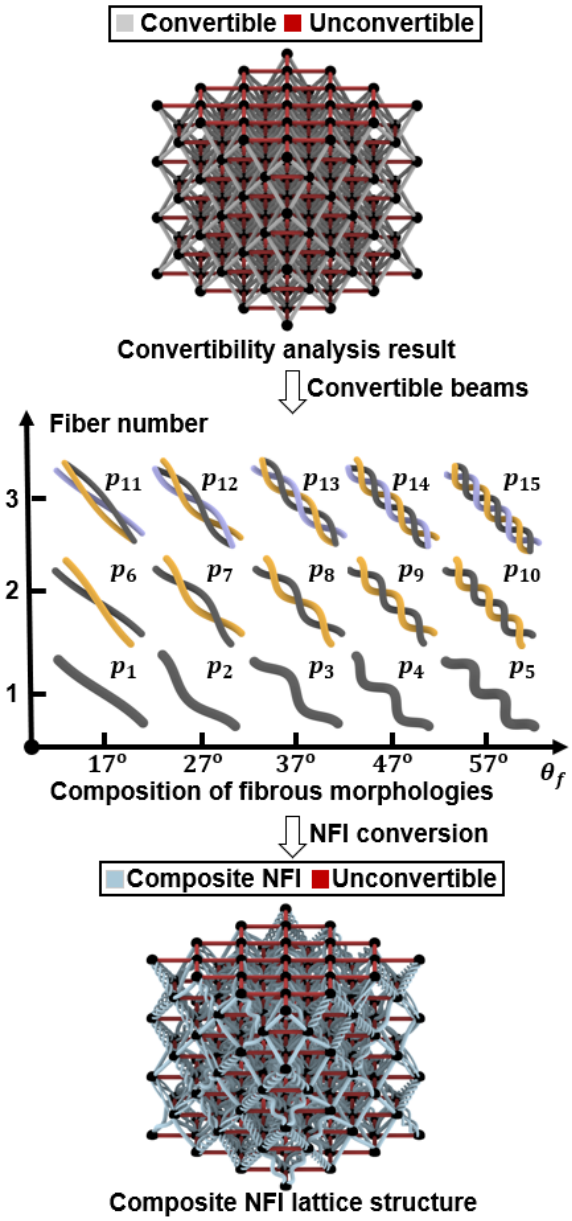

Fig. 10. The design of composite NFI octet-truss lattice of different percentages of fibrous morphologies (p_1 to p_{15}), where the fiber angle θ_f ranges from 17° to 57°, the fiber number n ranges from 1 to 3.

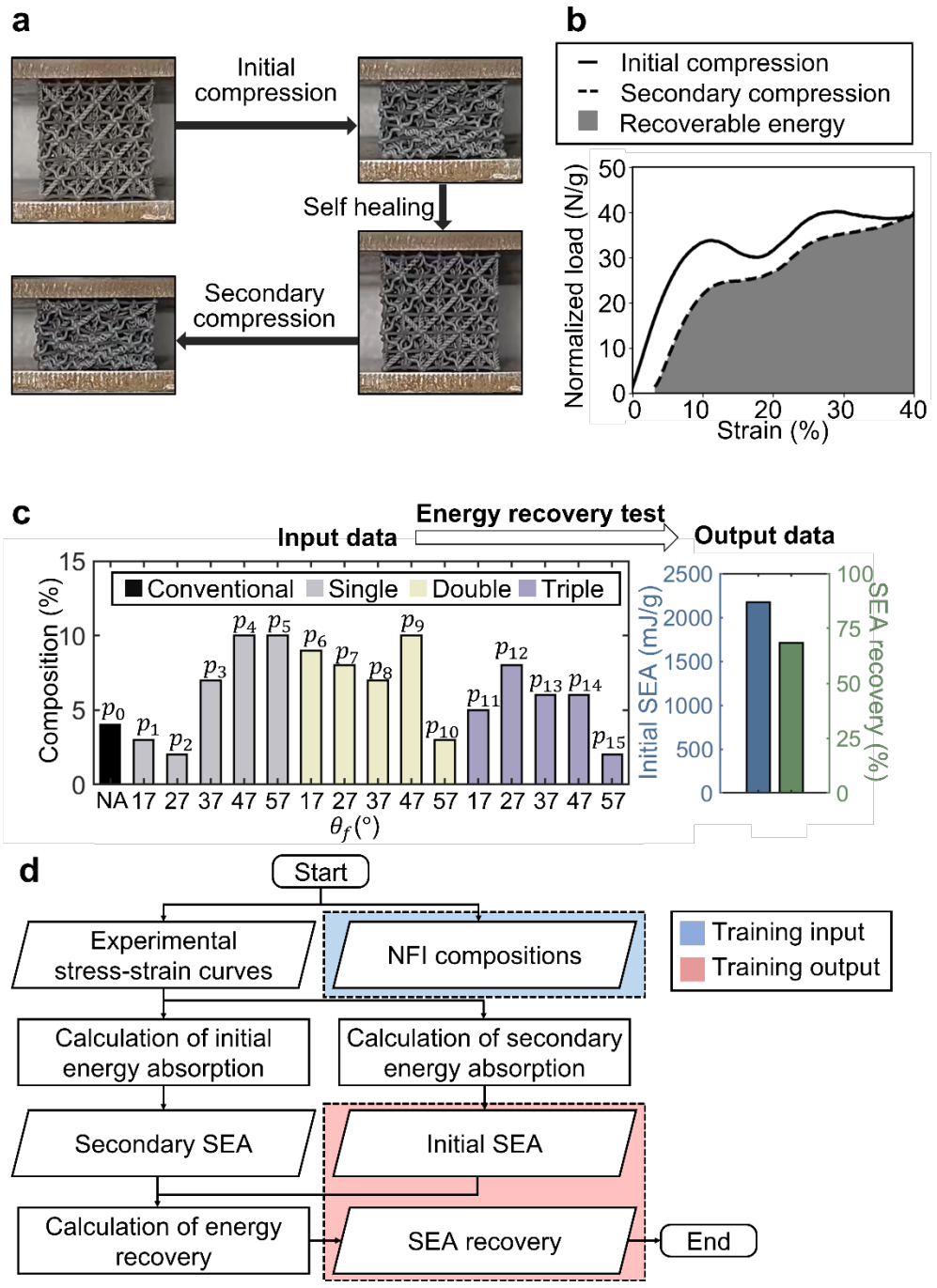

Fig. 11. The schematics of a sample training data: (a) the procedure of energy recovery test; (b) example initial and secondary compressive curves; (c) the constructed sample training data; (d) a flowchart of the processing of a sample training data.

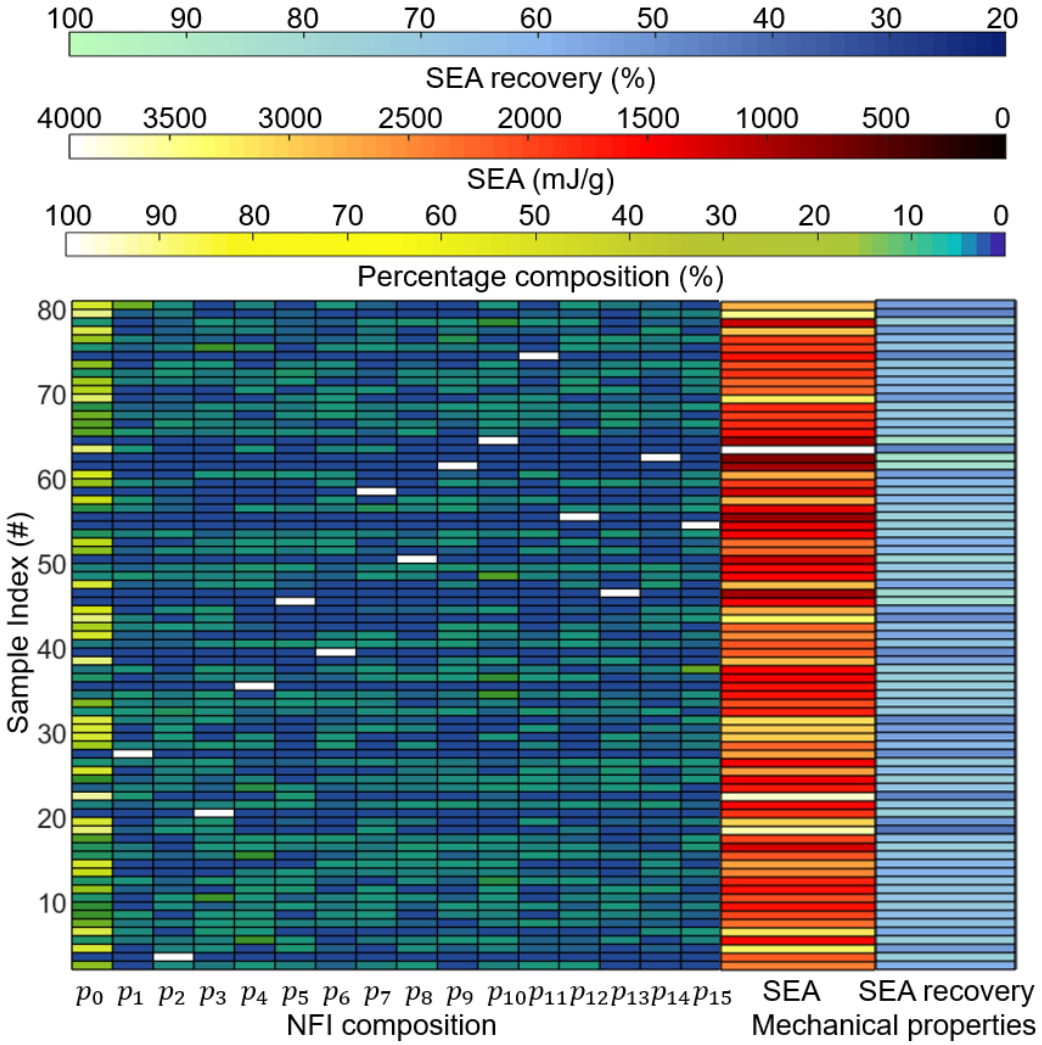

Fig. 12. The experimentally conducted training data.

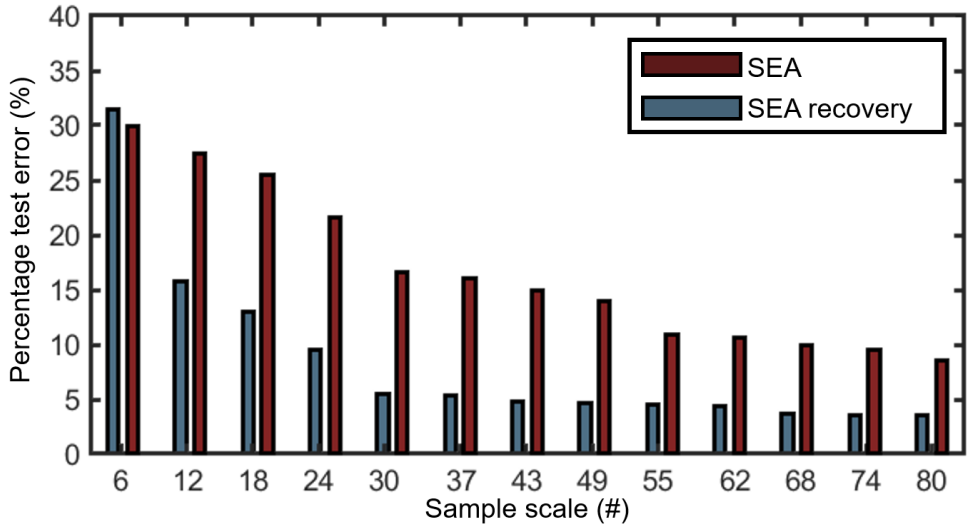

Fig. 13. The test errors of the FCNN for different numbers of the training data, where the confidence intervals of the FCNN are reflected in Fig. 16.

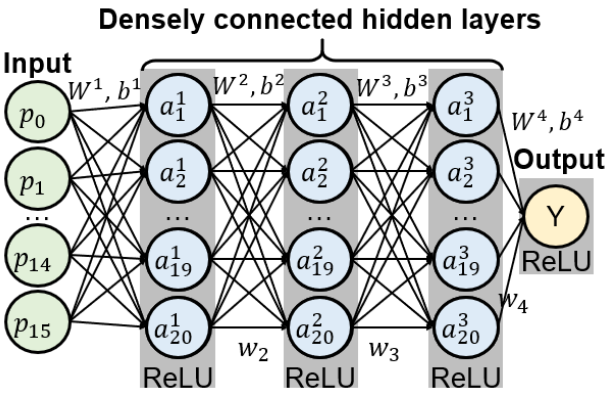

Fig. 14. The structure of FCNN, where Y represents the mechanical aspect to be predicted, a_j^i is the output values of the j^{th} neuron in i^{th} layer, W^i and b^i is the weight matrix and bias vector between the adjacent i^{th} and $i-1^{\text{th}}$ layer, respectively.

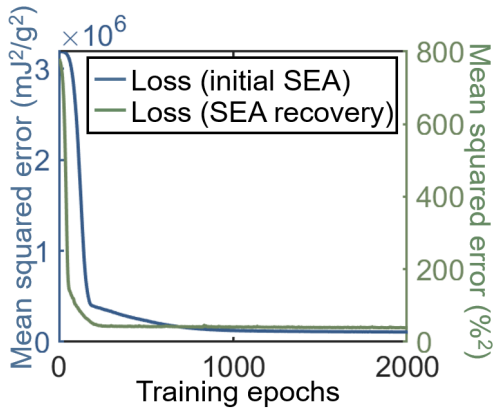

Fig. 15. The loss functions for initial SEA and SEA recovery during the training process.

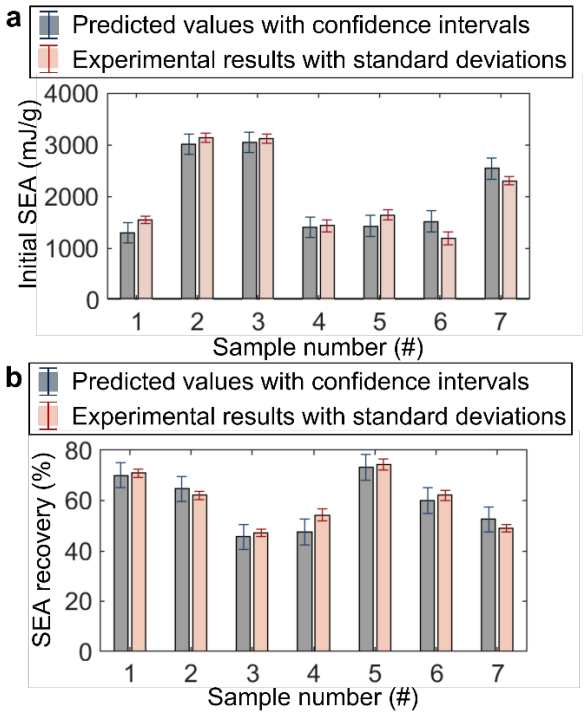

Fig. 16. Comparison between the FCNN-predicted (with confidence intervals) and experimentally observed (with standard deviations calculated based on three repetitive tests) initial SEA and SEA recoveries for the randomly selected test data.

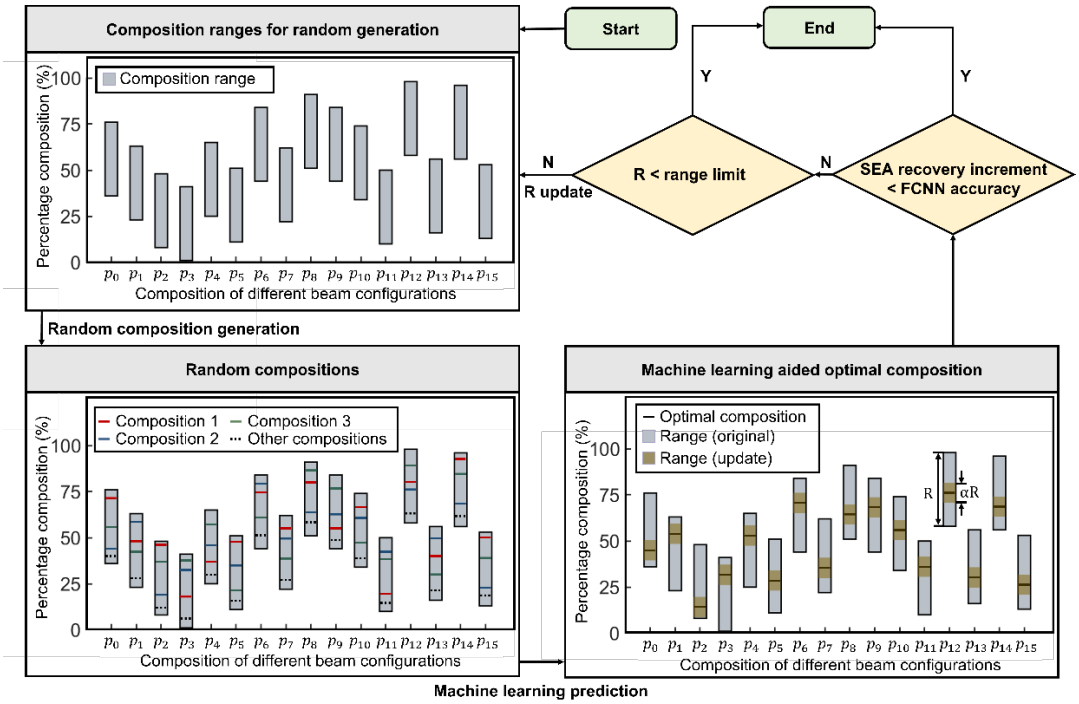

Fig. 17. A RGM deep search algorithm enabled by the ML prediction model, where R is the composition range of random- generation, α is the search-factor.

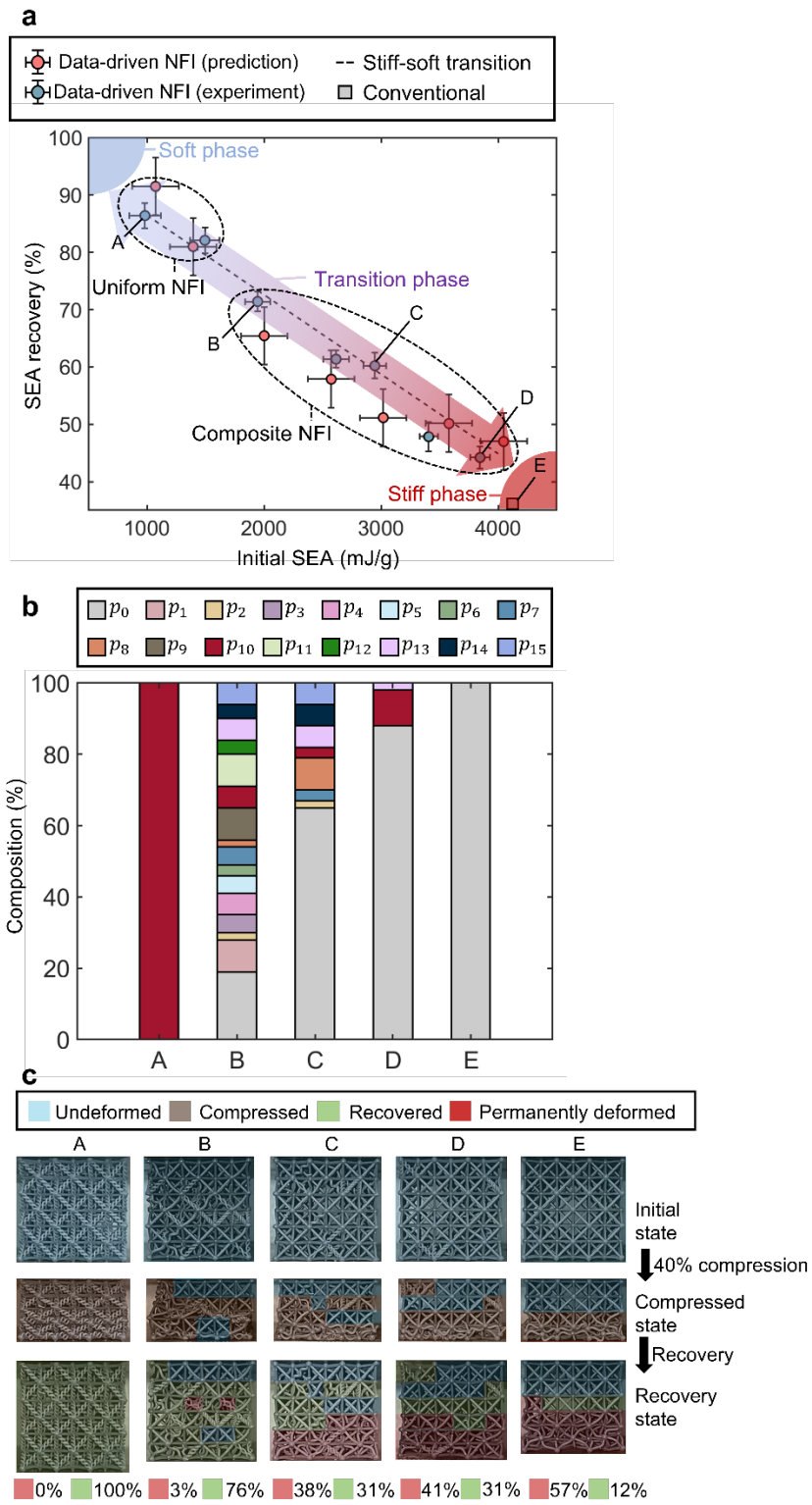

Fig. 18. The initial SEA and SEA recovery for data-driven NFI lattice material, and conventional octet-truss lattice material: (a) the experimental and predicted SEA recoveries and initial SEAs, where the error bars represents the confidence intervals and standard deviations (both scaled by 2) of the predicted and experimental data, respectively; (b) the fibrous composition of optimal NFI lattices (A-D) and conventional octet-truss lattice (E); (c) the experimentally observed compressive and recovery process.

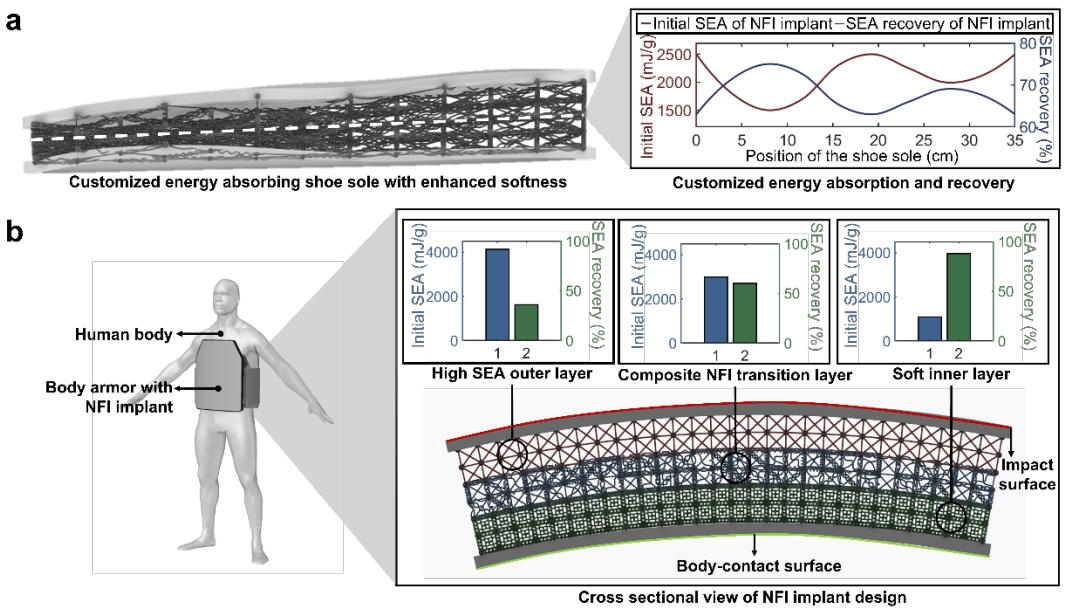

Fig. 19. Potential applications for the data-driven design of composite NFI octet-truss lattices: (a) a data-driven design of customized energy absorbing shoe sole design with artificially engineered balance of structural recovery and energy absorption performances; and (b) a layer-wise light-weight protective body armor with data-driven design of NFI implants.

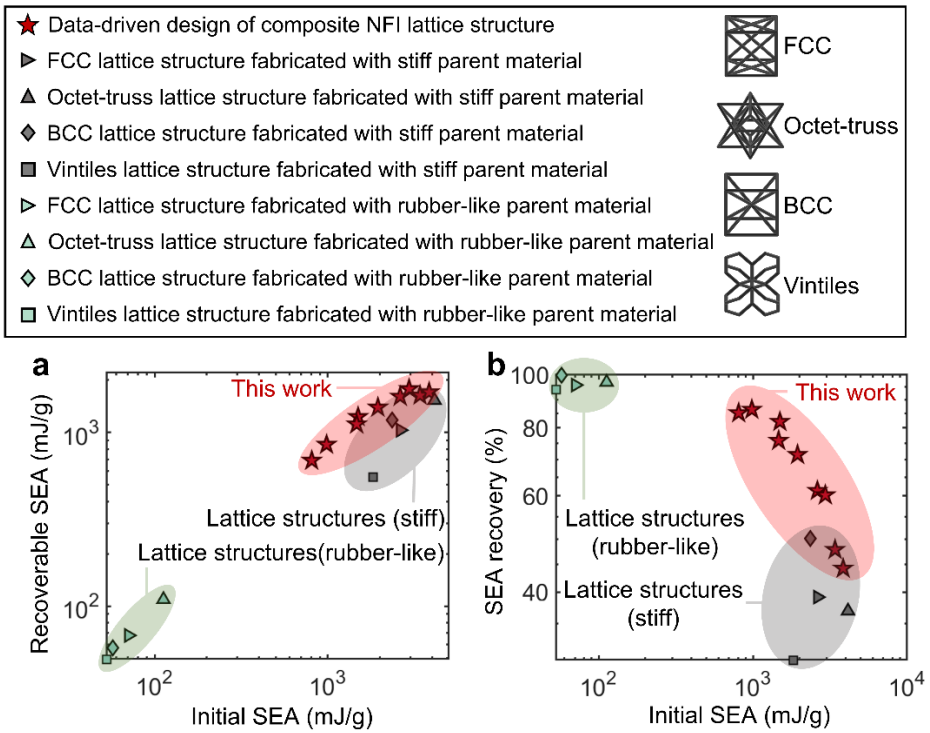

Fig. 20. Ashby chart reflecting (a) the recoverable SEA and initial SEA and (b) the SEA recovery ratio and initial SEA for data-driven NFI lattice material, and the state-of-the-art lattice structures built with stiff (Formlabs® Tough 2000) or rubber-like (Formlabs® Flexible 80A) parent materials.

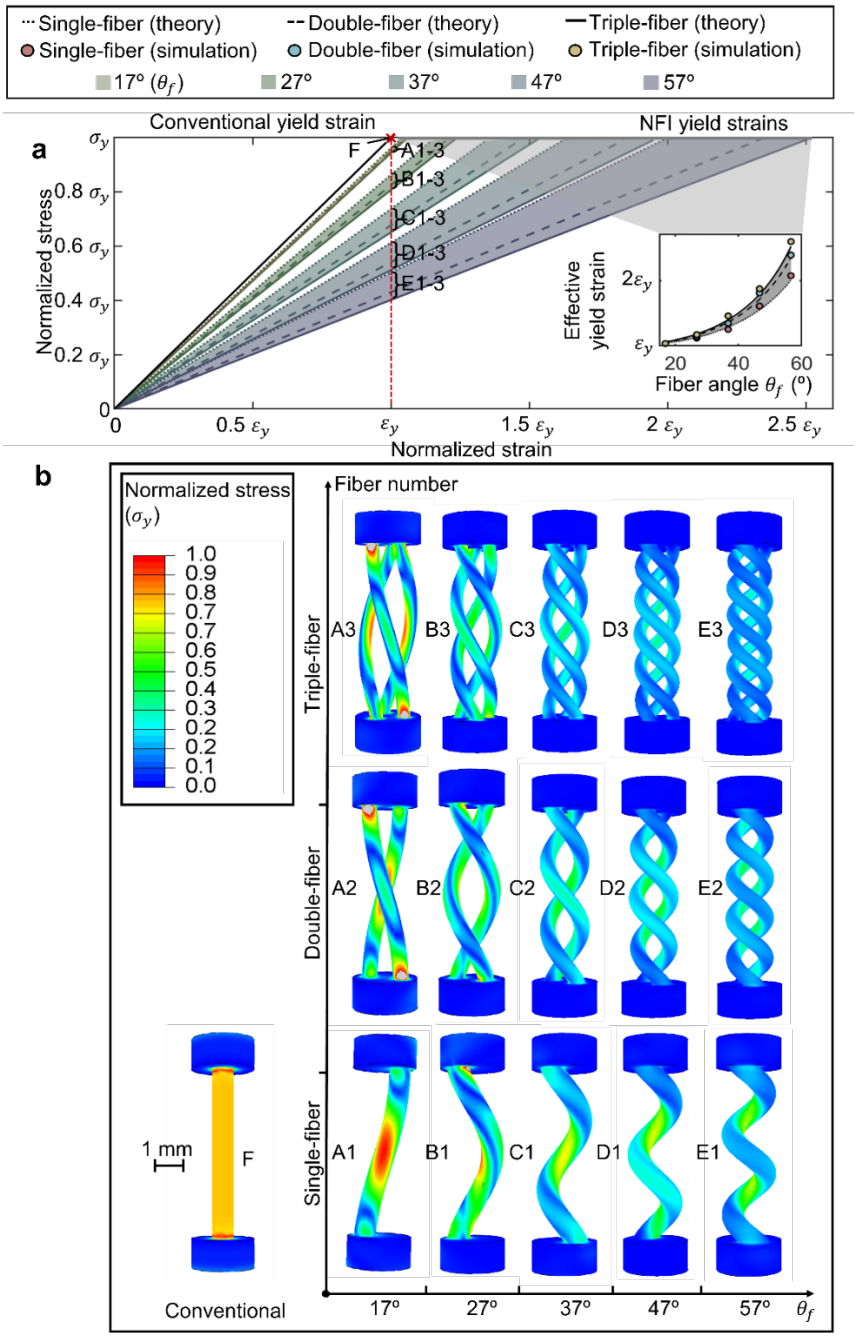

Fig. 21. Deformation and failure mechanisms of the conventional and NFI structs: (a) the theoretical $\boldsymbol{\varepsilon_y}$-normalized elastic mechanical performance of conventional and NFI structs with different fiber angles, $\boldsymbol{\theta_f}$, and fiber numbers, $\boldsymbol{n}$, where $\boldsymbol{\sigma_y}$ and $\boldsymbol{\varepsilon_y}$ represent the yield stress and strain for conventional structs, respectively; (b) the stress distribution of conventional and NFI structs deformed at conventional yield strain $\boldsymbol{\varepsilon_y}$, where A1-3 to E1-3 represents the NFI structs with different morphologies.

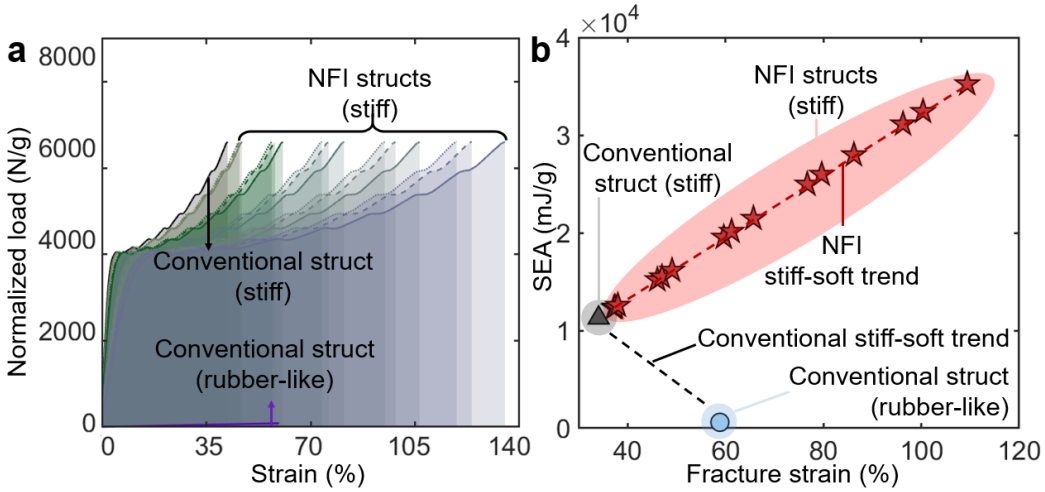

Fig. 22. The (a) theoretical elastoplastic behaviors and (b) SEA of the NFI structs built with stiff (Formlabs® Tough 2000) parent material, and the conventional structs prepared with both stiff and rubber-like (Formlabs® Flexible 80A) parent materials.

Table 1. The dimensions and mechanical properties of the tensile specimens.

Build material	Specimen number (#)	Test area (mm^2)	Modulus (MPa)	Yield stress (MPa)	Fracture stress (MPa)	Yield strain (%)	Fracture strain (%)
Formlabs® Tough 2000 resin	1	21.93	1303.88	26.01	37.96	3.46	34.10
	2	22.19	1306.31	25.97	30.85	3.45	31.96
	Average	22.06	1305.10	25.99	34.41	3.46	33.03
Formlabs® Flexible 80A resin	1	19.28	6.25	2.73	2.73	58.50	58.50
	2	19.12	4.59	2.24	2.24	59.23	59.23
	Average	19.20	5.42	2.49	2.49	58.87	58.87

Table 2. Design parameters of different fibrous morphologies.

Fiber morphology (#)	Fiber angle, θ_f (°)	Fiber number, n (#)
0	Conventional struct, not applicable	
1	17	1
2	27	1
3	37	1
4	47	1
5	57	1
6	17	2
7	27	2
8	37	2
9	47	2
10	57	2
11	17	3
12	27	3
13	37	3
14	47	3
15	57	3